



OPEN

Hyperpolarized ^{13}C -glucose magnetic resonance highlights reduced aerobic glycolysis in vivo in infiltrative glioblastoma

Mor Mishkovsky¹✉, Olga Gusyatiner^{2,3}, Bernard Lanz¹, Cristina Cudalbu⁴, Irene Vassallo^{2,3}, Marie-France Hamou^{2,3}, Jocelyne Bloch^{2,3}, Arnaud Comment⁵, Rolf Gruetter^{1,4,6,7} & Monika E. Hegi^{2,3}✉

Glioblastoma (GBM) is the most aggressive brain tumor type in adults. GBM is heterogeneous, with a compact core lesion surrounded by an invasive tumor front. This front is highly relevant for tumor recurrence but is generally non-detectable using standard imaging techniques. Recent studies demonstrated distinct metabolic profiles of the invasive phenotype in GBM. Magnetic resonance (MR) of hyperpolarized ^{13}C -labeled probes is a rapidly advancing field that provides real-time metabolic information. Here, we applied hyperpolarized ^{13}C -glucose MR to mouse GBM models. Compared to controls, the amount of lactate produced from hyperpolarized glucose was higher in the compact GBM model, consistent with the accepted “Warburg effect”. However, the opposite response was observed in models reflecting the invasive zone, with less lactate produced than in controls, implying a reduction in aerobic glycolysis. These striking differences could be used to map the metabolic heterogeneity in GBM and to visualize the infiltrative front of GBM.

Glioblastoma (GBM) is the most common malignant primary brain tumor in adults, notorious for its resistance to multimodal therapy with a median survival of less than 2 years¹. GBMs are characterized by genetic and morphologic intra-tumoral heterogeneity², and consist of a core lesion—often with central necrosis—surrounded by an invasive tumor front that is pivotal for tumor recurrence³. Within the standardized recommendations for imaging brain tumors⁴, the central mass can be detected by T_2 -weighted magnetic resonance imaging (MRI) and is highlighted in post-contrast T_1 -weighted image⁵. The infiltrative front, characterized by a low density of invading cells that have migrated into a region with an intact blood–brain barrier (BBB), is in contrast usually indiscernible with these standard MRI techniques. Consequently, part of it may lie outside of the resected and treated area following surgery and radiation therapy.

Metabolic imaging techniques can offer additional and essential information for the assessment of tumoral tissue⁶. Because upregulated glycolysis and the associated increase in lactate production (Warburg Effect) is considered a hallmark of cancer^{7,8}, glucose is the substrate of choice for metabolic imaging. Various techniques are available to study in vivo glucose metabolism non-invasively, giving complementary information on the metabolic pathways of glucose. The widely employed positron emission tomography (PET) of ^{18}F labeled fluoro-deoxyglucose (^{18}F -FDG)^{9,10} is limited to detect the total glucose consumption, without distinguishing between the tracer and its phosphorylated form, and cannot directly inform on the metabolic pathways subsequent to glucose phosphorylation. Moreover, the physiologic glucose consumption in the normal brain generates a high background uptake of ^{18}F -FDG, which is generally high in the gray matter, and moderate to high in the white matter, thus limiting its application for the detection of brain tumors¹¹. Magnetic resonance spectroscopy (MRS) of non-hyperpolarized (i.e. thermally polarized) metabolites allows to study brain tumor metabolism

¹Laboratory of Functional and Metabolic Imaging, École Polytechnique Fédérale de Lausanne (EPFL), Lausanne, Switzerland. ²Neuroscience Research Center, Lausanne University Hospital (CHUV) and University of Lausanne (UNIL), Lausanne, Switzerland. ³Service of Neurosurgery Lausanne, Lausanne University Hospital (CHUV) and University of Lausanne (UNIL), Lausanne, Switzerland. ⁴Center for Biomedical Imaging (CIBM), École Polytechnique Fédérale de Lausanne (EPFL), Lausanne, Switzerland. ⁵General Electric Healthcare, Chalfont St Giles, Buckinghamshire HP8 4SP, UK. ⁶Department of Radiology, University of Geneva (UNIGE), Geneva, Switzerland. ⁷Department of Radiology, University of Lausanne (UNIL), Lausanne, Switzerland. ✉email: mor.mishkovsky@epfl.ch; monika.hegi@chuv.ch

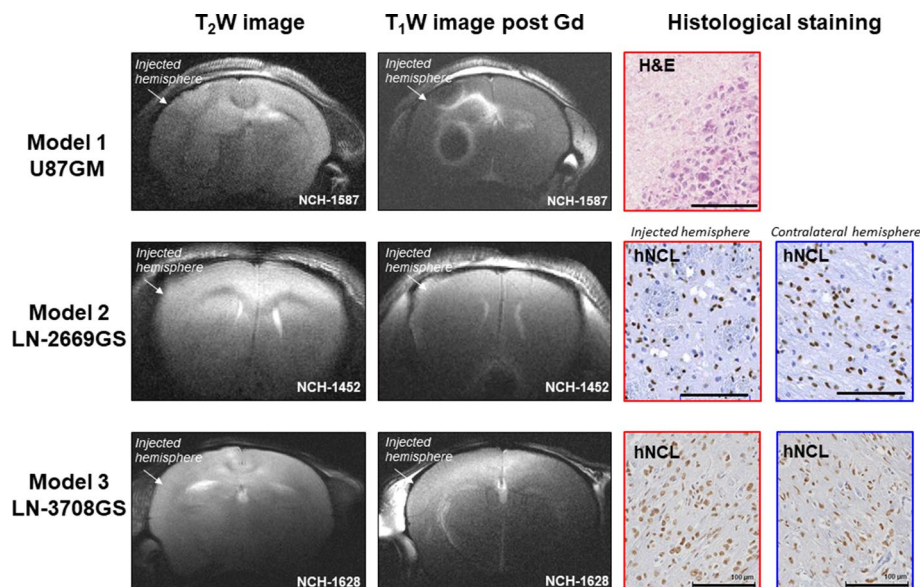


Figure 1. Axial slices of T₂-weighted images and T₁-weighted images post injection of gadolinium contrast agent. The arrows indicate the injected hemisphere. As expected, implantation of U87GM cells lead to the development of a focal tumor as confirmed by hematoxylin and eosin (H&E) staining (model 1). Immunohistochemistry for human Nucleolin (hNCL) that detects human cells, visualizing the highly invasive properties in the injected and the contra-lateral side in models 2 and 3, injected with LN-2669GS and LN-3708GS, respectively. NCH numbers indicate the identification number of each individual mouse.

non-invasively and with non-ionizing radiation^{12,13}. Metabolite concentrations that were quantified from ¹H MRS spectra were found to be changing in response to treatment and the metrics describing these characteristics are associated with survival. Moreover, metabolic abnormalities can be detected in the normal-appearing brain regions, emphasizing the potential of molecular imaging to visualize the infiltrative front^{14,15}. Nonetheless, despite recent developments, the applicability of these techniques with clinical diagnostics is still challenging. Good quality ¹H MRS spectrum requires high magnetic field homogeneity, and the measurement of the steady-state metabolite concentrations provides no direct information on metabolic fluxes. The dynamic measurements of non-hyperpolarized (i.e. thermally polarized) ¹³C MRS can bring kinetic information, but its low sensitivity necessitates long acquisition times and long infusion times.

MR detection of hyperpolarized (HP) endogenous compounds, on the other hand, using dissolution dynamic nuclear polarization (dDNP)¹⁶ can provide real-time metabolic information related to enzymatic activity¹⁷. The use of HP substrates has given important insights into GBM metabolism^{18–21}. In particular, MRS imaging of hyperpolarized [^{1-¹³C}] pyruvate has been shown as a promising technique to monitor metabolism in various clinical studies^{22,23} including brain tumor patients^{24–26}. HP pyruvate experiments are limited to probe a specific portion of the tumor glucose metabolism. The pyruvate bypasses the glucose transporters by entering the cell via the monocarboxylate transporters (MCTs) and then exchanges its ¹³C label with the endogenous lactate pools²⁷, providing a tool for lactate topography²². A recent metabolic study in a model representing the infiltrative front of GBM indicated a reduction in glucose uptake in the infiltrative GBM model as determined by PET, while the metabolic rate of glucose oxidation (CMRglc) quantified by non-hyperpolarized ¹³C MRS was not significantly reduced²⁸. Hence, direct detection of tumor glycolysis may provide new insights.

The possibility to directly monitor tumor glycolysis using hyperpolarized ¹³C labeled glucose has been demonstrated in a lymphoma mouse model in vivo²⁹. We have recently reported the real-time detection of cerebral de novo synthesis of [^{1-¹³C}]lactate following the infusion of HP [²H₇, ¹³C₆]D-glucose in mice³⁰. Therefore, the aim of this study was to demonstrate the feasibility to monitor real-time metabolism of hyperpolarized [²H₇, ¹³C₆]D-glucose in GBM mouse models and to employ this technique to further investigate the metabolic fate of glucose in the infiltrative zone of GBM of patient-derived xenografts in mice. We aimed to address the question of whether changes in glucose metabolism can be characterized by measuring the de novo lactate production through glycolysis, and whether these can delineate differences between the invasive zone of GBM from the normal brain by real-time detection of glycolysis.

Results

Implantation of the U87GM cell line (model 1) yielded a compact tumor. A contrast-enhancing ring around a necrotic core can be readily observed in the post-contrast T₁-weighted images, indicative of BBB disruption. Histology confirmed the observations of a compact tumor in the MRI images (Fig. 1). The patient-derived LN-2669GS (model 2) and LN-3708GS (model 3) sphere lines gave rise to diffusely invading tumors without visible modifications of the brain structure, and were characterized by lack of a focal mass, and absence of enhancement

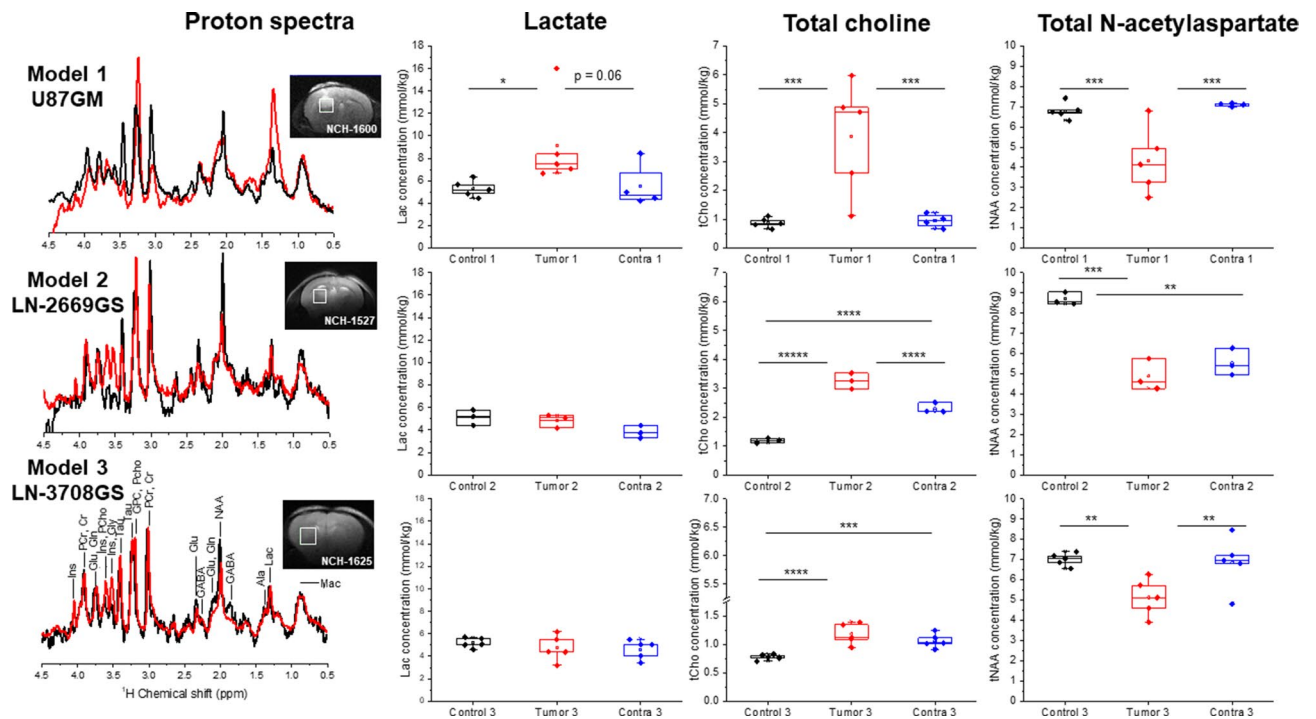


Figure 2. The steady-state concentrations of lactate, total choline (tCho) and total *N*-acetylaspartate (tNAA) concentrations at the day of HP glucose infusion. Localized ^1H spectra were acquired in an $8\ \mu\text{L}$ voxel, located in the cell injected hemisphere, as designated by the white square in the image (red spectra), corresponding voxel in the contralateral hemisphere (not shown) and in similar voxel in control animals (black spectra). The presented concentrations are only from the animals that received the HP ^{13}C glucose bolus. In black are concentrations in the medium injected hemisphere in controls (control 1–3). In red, are concentrations in the tumor cell injected hemisphere (tumor 1–3), and in the blue concentrations in the contralateral hemisphere (contra 1–3) respectively. The number of * represent statistically significant levels of $p=0.05$, 0.01 , 0.005 , 0.001 , 0.0005 and 0.00005 . NCH numbers indicate the identification number of each individual mouse.

after gadolinium injection. Human tumor cells, visualized by immunostaining for human nucleolin, displayed highly invasive features, infiltrating also the contralateral hemisphere (Fig. 1).

Metabolic profiling of tumor models. The metabolite concentrations derived from the ^1H spectra resulted in distinct metabolic profiles of the tumor models as compared to the contralateral hemisphere and their corresponding controls (Fig. 2). The changes in cerebral metabolite concentrations enabled us to monitor the development of the infiltrative tumors post cell implantation and to sense cell migration to the contralateral hemisphere (Supporting Information Figure 1). In all three examined GBM models, the tumor tissue showed an increase in the concentration of total choline (tCho) metabolites that are related to membrane degradation and cell proliferation. The putative neuronal marker tNAA showed decreasing concentrations in all developing tumors of the injected hemispheres as well as in the contralateral hemispheres of the mice injected with the highly infiltrative model 2. The lactate pool size increased in model 1 in the area of the compact tumor mass but did not change in the infiltrative GBM models i.e. models 2 and 3 (Fig. 2).

Real-time measurement of hyperpolarized glucose metabolism. The infusion of HP [$^2\text{H}_7, ^{13}\text{C}_6$] glucose led to the production of [$1-^{13}\text{C}$] lactate. The area under the curve (AUC) of [$1-^{13}\text{C}$] lactate (183.5 ppm), [$1-^{13}\text{C}$] α -glucose (92.9 ppm), and [$1-^{13}\text{C}$] β -glucose (96.8 ppm) were quantified using VNMRJ software by integrating the sum of the ^{13}C MRS spectra after phase and baseline correction. The lactate-to-glucose ratio (LGR) between the [$1-^{13}\text{C}$] lactate signal and the sum of [$1-^{13}\text{C}$] α - and β -glucose was calculated. The exact concentration of the glucose at the infusate solution was determined by high-resolution ^{13}C NMR as previously proposed³¹. To account for the difference between animals and variances in infusate concentrations post dissolution, we multiplied those ratios by the actual concentration of the injected HP glucose divided by the animal blood volume, resulting in a corrected-LGR (cLGR) as previously described³². As anticipated, in the well characterized U87GM model (model 1) the [$1-^{13}\text{C}$] lactate signals were higher in the tumor bearing brains compared to their controls, with the calculated cLGR being 29% higher ($p=0.009$) in the tumor bearing mice. Interestingly, an opposite trend was observed in the infiltrative GBM models 2 and 3, in which the signals of [$1-^{13}\text{C}$] lactate after the HP ^{13}C glucose bolus were smaller than in their corresponding healthy controls, respectively. The cLGR were reduced by 65% and 48% in the infiltrative models 2 and 3, respectively, as compared to their controls (Fig. 3). This difference was significant in model 3 ($p=0.001$), however did not reach statistical significance in model 2 ($p=0.113$).

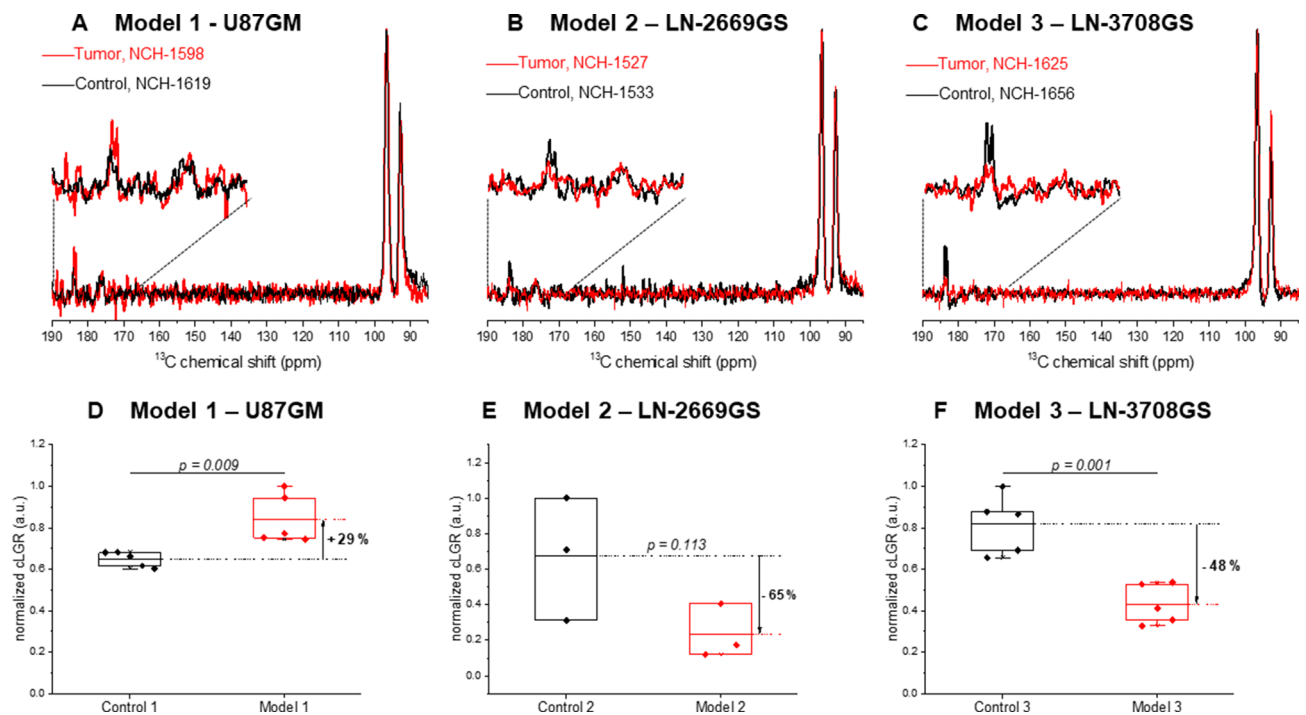


Figure 3. In vivo ^{13}C magnetic resonance spectroscopy (MRS) of hyperpolarized glucose. (A–C) Characteristic summed spectra measured from the different tumor models over both hemispheres (red) and the corresponding controls (black) following a bolus of hyperpolarized (HP) $[\text{2H}_7, \text{13C}_6]$ D-glucose (A–C). Spectra are normalized to their maximal glucose signal, respectively. In all acquisitions $[1\text{-}^{13}\text{C}]$ D-glucose- β (96.8 ppm), $[1\text{-}^{13}\text{C}]$ D-glucose- α (92.9 ppm) and $[1\text{-}^{13}\text{C}]$ Lactate (183.5 ppm) were detected. The broad peak at 175 ppm (designated by a star) is an impurity in the $[\text{2H}_7, \text{13C}_6]$ D-glucose powder. (D–F) A comparison cLGR revealed an increase in the cLGR in model 1 compared to its control, and a decrease of the cLGR in infiltrative models (2 and 3) compared to the corresponding controls. cLGRs are normalized to the maximum cLGR observed in each pair to account for the differences in animals' stains and age between the groups (Supporting Information Table 1). For all the measurements, we calculated blood glycaemia of 20.2 ± 3.6 mM and fractional enrichment of ^{13}C glucose was $53.8 \pm 10.2\%$, with no significant differences between the groups (Supporting Information Figure 3). NCH numbers indicate the identification number of each individual mouse.

The latter may be due to the small number of mice, and the slightly lower ^{13}C fractional enrichment of glucose in the control 2 animals (Supporting Information Figure 3). Note that blood glycaemia and ^{13}C glucose fractional enrichment that may influence these ratios were kept similar for all different measurements, and showed no significant differences between the groups (Supporting Information Figure 3).

Discussion

Recent ex vivo and in vivo studies have shown evidences for distinct metabolic profiles associated with the invasive phenotype in GBM, indicating active glucose oxidation in human GBM^{28,33}. In this work, we applied, for the first time, HP ^{13}C labeled-glucose to further investigate glucose metabolism in GBM xenograft models in the mouse. The cLGR calculated from this measurement is connected to the rate of glucose uptake and real-time lactate production through glycolysis^{29,30}. We examined three GBM models, two representing the infiltration zone (models 2 and 3), and are similar to the ones studied by Lai et al.²⁸, and the U87GM model that leads to the formation of focal GBM mass (model 1). The latter is a well-characterized GBM model and was employed in this study to validate the reliability of the metabolic information detected by the cLGR from the HP glucose MRS. Namely, U87GM forms hypoxic tumors³⁴, as such, hypoxia-induced factor 1 (HIF1) activates genes involved in extracellular glucose import and thus stimulating glycolytic energy production^{35,36}. This was previously visualized by hyperintensity in ^{18}F -FDG imaging³⁷ and an increase in the endogenous lactate pool-size^{34,38} (Fig. 2). The HP ^{13}C glucose MRS detection of a significantly higher cLGR in brains of U87GM mice (model 1) compared to control (control 1) was thus consistent (Fig. 3, +29%, $p=0.009$), and is in accordance with the metabolic shift anticipated by the so-called 'Warburg Effect'^{7,8}. Moreover, this higher labeling of lactate is consistent with previous studies with HP $[1\text{-}^{13}\text{C}]$ pyruvate in the U87GM tumor model that showed a high level of $[1\text{-}^{13}\text{C}]$ lactate labeling³⁹.

Interestingly, in models 2 and 3, which reflect the infiltration zone of GBM, we found a different behavior of the cLGR. In model 3 the cLGR in the tumor bearing mice was significantly lower than in the corresponding controls (–48%, $p=0.001$), and in model 2 the same trend was observed (–65%) without reaching statistical significance. Based on the cLGR values we found that de novo synthesis of lactate as detected by HP glucose MRS, was actually lower in the brains of mice implanted with the infiltrative models compared to their corresponding healthy controls. This indicates a reduction of aerobic glycolysis in infiltrative GBM, thus showing an

opposite trend to what would be expected by the so-called ‘Warburg effect’. Previous work on patient-derived GBM models, has reported on a link between ^{13}C labelling of lactate from a HP [$1\text{-}^{13}\text{C}$] pyruvate bolus and c-Myc expression⁴⁰. Upregulation of c-Myc may result in upregulation of GLUT1, MCT1, HK, and LDHA, thus one could anticipate a higher lactate labeling from both HP [$1\text{-}^{13}\text{C}$] pyruvate and HP ^{13}C glucose under c-Myc upregulation⁴¹. In light of that, lower lactate labelling from the HP glucose may be related to lower c-Myc expression in the infiltrative models studied in the present work. However further investigations are necessary to confirm this hypothesis. Moreover, in these tumors, the endogenous lactate pool size was similar to controls, in line with the absence of hypoxic conditions, as we have previously reported²⁸. In addition, the labeling of [$3\text{-}^{13}\text{C}$] lactate, after continuous infusion of thermally polarized [$1,6\text{-}^{13}\text{C}_2$] glucose, was similar in the infiltrative tumor model as compared to the control brain²⁸. One could anticipate a similar response to a long infusion of thermally polarized [$6,6'\text{-}^2\text{H}_2$] glucose^{42,43}. Thus the discrepancy between the lactate pool size and lactate labeling emphasizes the unique contrast one can detect with HP ^{13}C glucose MRS, which enables monitoring the net ^{13}C lactate production. It is likely that the reduction in the cLGR observed here, is a consequence of a decrease in the uptake of glucose. The present results support the work of Lai et al. on similar infiltrative GBM models, which indicated a reduction in glucose uptake as determined by ^{18}F -FDG PET imaging, while the metabolic rate of glucose oxidation (CMR_{glc}) quantified by ^{13}C MRS was not significantly reduced²⁸. Moreover, recent studies with HP pyruvate reported that although the lactate pool does play a role in the hyperpolarized lactate signal²⁷, the pyruvate transport via MCT is of a major role in the detection of downstream metabolites post HP pyruvate bolus in some tumors^{44–46}. A further step would be to examine perhaps a similar outcome might be possible with HP ^{13}C -pyruvate in the infiltrative models investigated here. Of note, in the summed spectra of all the different models investigated in this study, we could only detect the resonances of the infused HP glucose and the produced lactate (Supporting Information Figure 4). Nonetheless, we cannot exclude the possibility that HP glucose was directed to the pentose phosphate pathway (PPP) to sustain proliferation by the production of amino acids, thus resulting in a reduction in the de novo synthesis of ^{13}C labelled lactate. It is likely that the sensitivity of the current approach of using HP glucose can be further improved by optimal sample formulation²¹ or utilization of specifically labelled glucose³⁰, and may lead to the observation of additional metabolites that could shed light on the metabolic pathway involved in the observed reduction in aerobic glycolysis.

The global acquisition strategy employed in this study probably led to an underestimation of the differences between the tumor metabolism of HP glucose in the brains implanted with U87GM tumor cells and respective mock injected control brains. The global detection scheme employed here confounds the possibility to define the metabolic response solely of the tumor tissue. The sensitive area under the coil likely was not only composed of tumor tissue (Supporting Information Figure 2). However, even using this somewhat limited detection mode, all measured parameters are coherent with what is anticipated by the Warburg effect in this well-characterized model. A localized detection scheme would indeed be preferable, and would enable discrimination between the tumor and the surrounding brain, and would eventually yield even more pronounced differences. For the infiltration models (models 2 and 3), the tumor cells diffused in the brain tissue (Fig. 1), hence the limitation in localization is inherent to these models, consequently, a localized detection would lead to a similar result to what we observed here by the global detection scheme.

Despite limitations of our acquisition strategy and the restricted number of animals, our results provide proof-of-principle evidence for the possibility of using HP [$^2\text{H}_7, ^{13}\text{C}_6$] D-glucose to monitor lactate production in brain tumors. The need for novel techniques to visualize the invasive front of glioblastoma is well established. Here we demonstrate that the amount of freshly synthesized [$1\text{-}^{13}\text{C}$] lactate produced after exogenous HP [$^2\text{H}_7, ^{13}\text{C}_6$] D-glucose bolus is increased in the compact GBM tumor model, but decreased in the infiltrative GBM models as compared to their respective controls. Although technical challenges need to be overcome before introducing the cLGR in diagnostic imaging as a metabolic contrast and in particular limitations related to the short lifetime of the hyperpolarized state of glucose, it brings the potential to visualize the infiltrative front of GBM, displaying hyperintensity in the compact tumor part and hypointensity at the infiltrative front, a compartment highly relevant for tumor recurrence. Recent developments around photo-induced radicals have opened opportunities to reduce the delay between preparation and injection of hyperpolarized substrates, possibly allowing translation of hyperpolarized ^{13}C -glucose^{47–49}.

Conclusion

We applied for the first time HP glucose MRS to study glucose metabolism in brain tumors, and found a reduction in aerobic glycolysis in a GBM model representing the infiltrative zone, in opposition to what is expected by the ‘Warburg effect’.

Methods and materials

Animal experimentation. Experiments were performed according to the Swiss law for the protection of animals and were approved by the Veterinary Office of the Canton de Vaud (Service de la consommation et des affaires vétérinaires, VD1181.6, VD2777, and VD3266). All experiments were conducted according to federal and local ethical laws and complied with the ARRIVE guidelines. Mice were given free access to food and water and were maintained in a 12 h light–dark cycle in a temperature- and humidity-controlled animal facility.

Orthotopic mouse glioma xenograft models. To evaluate the metabolic performance of HP glucose MRS, the well-characterized U87GM GBM model was employed. U87 cells (10^5), obtained from ATCC, were stereotactically injected into the left hemispheres of immunodeficient mice. This model will be referred to as model 1. To model the infiltrative compartment of GBM, the patient-derived glioblastoma sphere lines (GS) LN-2669GS (clone 822, n = 2; clone 867, n = 1)^{50,51} and LN-3708GS were stereotactically injected into the left

hemispheres of immunodeficient mice as previously described (10^5 cells in 5 μ L Hank's Balanced Salt Solution, HBSS)⁵², and will be referred to as Model 2 and 3, respectively. The GS lines were established in the laboratory with written consent of the patients (protocol F25/99, approved by the local ethics committee), and authenticated together with the original tumors using short tandem repeats (STR) (Dr. Vincent Castella, University Center of Legal Medicine, Lausanne, Switzerland). The corresponding controls (i.e. control 1, 2, and 3) were orthotopically injected with 5 μ L of the cell suspension solution (HBSS) solely. All mice were 6 weeks old at the time of cell implantation. The age at the final HP ^{13}C MRS measurement was dependent on the latency of tumor development and varied between the three models. Overall, 31 mice were employed in this study, among them 18 mice were injected with tumor cells and 13 mice were injected with the cell medium for control. Baseline information for the different groups is summarized in Supplementary Table 1.

Hyperpolarization. HP of ^{13}C -labelled glucose was prepared as previously described³⁰. Briefly, [1,2,3,4,5,6,6- $^2\text{H}_7$, U- $^{13}\text{C}_6$]D-glucose (Sigma Aldrich) was dissolved in a polarization medium containing trityl radical OX63 (tris{8-carboxyl-2,2,6,6-benzo(1,2-d:5-d)-bis(1,3)dithiole-4-yl-methyl sodium salt) as a polarizing agent (ALBEDA, Denmark) dissolved in deionized water with 1:1.1 (w/w) ratio, to yield 3 M glucose and 25 mM OX63 radical solution. Frozen beads of the solution were dynamically polarized in a custom-designed 7 T DNP polarizer operating at 197 GHz/ 1.00 ± 0.05 K³³ for 3 h, and then rapidly dissolved in 5 mL of superheated D_2O and transferred within 2 s into the separator/infusion pump⁵⁴, which was prepositioned inside the magnet bore. A bolus of the solution was then automatically infused through a vein catheter (see below) to the mouse as previously described³¹.

Animal preparation for magnetic resonance scans. Mice were longitudinally scanned to monitor tumor development. Tumor bearing or control mice were anesthetized using $1.5 \pm 0.5\%$ isoflurane (Attane, Minrad, NY, USA) in 60% oxygen using a facemask. The anesthetized animals were then transferred to an MRI bed, and their head was fixed using a stereotaxic system and a bite bar (RAPID Biomedical Inc., OH, USA). Animal physiology was monitored during the entire duration of the experiment. Body temperature was monitored by a nonmagnetic rectal probe and maintained at 37.0 ± 0.5 °C by warming the animal with temperature-controlled water circulation (SA instruments Inc. NY, USA). The respiration rate was monitored using a pneumatic pillow sensor (SA Instruments Ins. Stony Brook, NY, USA).

Mice were selected for the HP glucose experiment when their physiology (i.e. weight loss), as well as MRI images and/or metabolites concentration from the MRS spectra indicated presence of a tumor (evolution of some metabolites in infiltrative models is presented in Supporting Information Figure 1). At the day of the HP glucose experiment, the anesthetized animals were cannulated. In experiments with models and controls 1 and 3, the catheter was positioned in the femoral vein. In experiments with model 2 and corresponding control 2, the tail vein was catheterized to deliver hyperpolarized glucose solution. After mice were transferred to the MRI bed, blood glycaemia levels were measured from blood samples (5 μ L) collected from the tip of the tail (Breeze2 glucose meter, Bayer, France), and the animals were entered into the MR scanner.

All MR measurements were carried out on a Varian INOVA spectrometer (Agilent, Palo Alto, CA, USA) interfaced with a 31-cm horizontal-bore actively shielded 9.4 T magnet (Magnex Scientific, Abingdon, UK).

In vivo ^1H magnetic resonance imaging and spectroscopy. To confirm the presence of tumor we searched for morphological modifications ($T_2\text{W}$ images) and/or changes in the neurochemical profiles (localized ^1H MRS). Spectra were acquired every second week starting 4 weeks post cell implantation. Measurements were performed using a home-built ^1H -quadrature surface coil that was placed on top of the mouse head. $T_2\text{W}$ images were acquired using a fast spin echo multi slice (FSEMS) protocol (FOV 18×18 mm², TR=4000 ms, effective TE=52 ms, 6 scans). B_0 inhomogeneity was corrected using the FASTESTMAT algorithm⁵⁵ in two $2 \times 2 \times 2$ mm voxels, one located in the cell injection area, and the other one located in the corresponding area of the contralateral hemisphere. The positioning of the tumor voxel was guided by the location of the scar that was formed post cell implantation. Cells were injected at the same coordinates relative to the Bregma by means of a stereotaxic frame, thus, this voxel is always located at the same general position. The contralateral voxel was taken as the mirror image of the tumor voxel. ^1H MRS measurements were acquired using SPECIAL pulse sequences⁵⁶ (TR=4000 ms, TE=2.8 ms, 200 ms acquisition time in 15×16 scans). Absolute metabolite concentrations were calculated using LC Model⁵⁷.

The integrity of the blood–brain barrier (BBB) was assessed only on the day of the final experiment by T_1 weighted ($T_1\text{W}$) imaging post-injection of gadolinium contrast agent gadolinium (Gd3+) dihydroxy-hydroxyethylpropyl-tetraazacyclododecane-triacetic acid (Gadovist, Bayer Pharmaceuticals, France, 5 μ L/g body weight). This procedure was done after the completion of the HP ^{13}C MRS measurements, using FSEMS pulse-sequence (FOV 18×18 mm², TR=350 ms, effective TE=11 ms, 6 averages).

In vivo hyperpolarized ^{13}C MRS. ^{13}C MR measurements were performed using a home-built ^1H -quadrature/ ^{13}C -single loop surface coil that was positioned on top of the mouse head. To improve the detection within the sensitive area of the ^{13}C coil (Supporting Information Figure 2), B_0 inhomogeneity was corrected using FASTESTMAP algorithm⁵⁵ in a 135 μ L voxel. A 540 μ L of 59 ± 17 mM HP [$^2\text{H}_7$, $^{13}\text{C}_6$]D-glucose was injected through a vein catheter by the automated protocol³¹. A series of pulse acquired sequences was then triggered 5.5 s post injection every 0.5 s for 50 s. Frequency selective Gaussian pulse (250 μ s) was centered at 182 ppm resulting an average nominal 20° flip-angle of the C1 lactate resonance (183.5 ppm) and 1.4° flip-angle on the glucose C1 resonances (92.9 ppm and 96.8 ppm) as previously proposed³⁰. The area under the curve (AUC) of [$1\text{-}^{13}\text{C}$] lactate (183.5 ppm), [$1\text{-}^{13}\text{C}$] α -glucose (92.9 ppm), and [$1\text{-}^{13}\text{C}$] β -glucose (96.8 ppm) were quantified

using VNMRJ software by integrating the sum of the ^{13}C MRS spectra after phase and baseline correction. Overall, 13 tumor mice, and 13 control mice received the HP glucose bolus (model 1, $n = 5$; control 1, $n = 5$; model 2, $n = 3$; control 2, $n = 3$; model 3, $n = 5$; control 3, $n = 5$).

Histology and immunohistochemistry. Brains were fixed in formalin (4% buffered formalin), and embedded in paraffin. Coronal sections were stained by H&E (haematoxylin and eosin) or immunostained for human nucleolin (hNCL, 1:200, 4 °C, overnight; ab13541, Abcam, Cambridge, UK; does not react with mouse) to visualize the human GBM cells using a heat antigen retrieval procedure as previously described⁵⁸.

Statistical analysis. Statistical analyses were performed using the OriginPro 9.3G software. One-way analysis of variance (1-way ANOVA) was used followed by Fisher's test to find significance in the difference between each tumor and its corresponding control. A p value of 0.05 was considered significant. All data are presented as means \pm standard deviation unless otherwise stated.

Data availability

All data is available from the corresponding authors upon reasonable request.

Received: 10 July 2020; Accepted: 28 February 2021

Published online: 11 March 2021

References

- Stupp, R. *et al.* Effect of tumor-treating fields plus maintenance temozolomide vs maintenance temozolomide alone on survival in patients with glioblastoma: A randomized clinical trial. *JAMA* **318**, 2306–2316. <https://doi.org/10.1001/jama.2017.18718> (2017).
- Sottoriva, A. *et al.* Intratumor heterogeneity in human glioblastoma reflects cancer evolutionary dynamics. *Proc. Natl. Acad. Sci. U.S.A.* **110**, 4009–4014. <https://doi.org/10.1073/pnas.1219747110> (2013).
- Lan, X. *et al.* Fate mapping of human glioblastoma reveals an invariant stem cell hierarchy. *Nature* **549**, 227–232. <https://doi.org/10.1038/nature23666> (2017).
- Ellingson, B. M. *et al.* Consensus recommendations for a standardized Brain Tumor Imaging Protocol in clinical trials. *Neuro Oncol.* **17**, 1188–1198. <https://doi.org/10.1093/neuonc/nov095> (2015).
- Kalpathy-Cramer, J., Gerstner, E. R., Emblem, K. E., Andronesi, O. & Rosen, B. Advanced magnetic resonance imaging of the physical processes in human glioblastoma. *Cancer Res.* **74**, 4622–4637. <https://doi.org/10.1158/0008-5472.CAN-14-0383> (2014).
- Ntzachristos, V., Pleitez, M. A., Aime, S. & Brindle, K. M. Emerging technologies to image tissue metabolism. *Cell Metab.* **29**, 518–538. <https://doi.org/10.1016/j.cmet.2018.09.004> (2019).
- Warburg, O. On the origin of cancer cells. *Science* **123**, 309–314. <https://doi.org/10.1126/science.123.3191.309> (1956).
- Hanahan, D. & Weinberg, R. A. Hallmarks of cancer: The next generation. *Cell* **144**, 646–674. <https://doi.org/10.1016/j.cell.2011.02.013> (2011).
- Phelps, M. E. *et al.* Tomographic measurement of local cerebral glucose metabolic rate in humans with (F-18)2-fluoro-2-deoxy-D-glucose: Validation of method. *Ann. Neurol.* **6**, 371–388. <https://doi.org/10.1002/ana.410060502> (1979).
- Huang, S. C. *et al.* Noninvasive determination of local cerebral metabolic rate of glucose in man. *Am. J. Physiol.* **238**, E69–82. <https://doi.org/10.1152/ajpendo.1980.238.1.E69> (1980).
- Sharma, A. & McConathy, J. Overview of PET tracers for brain tumor imaging. *PET Clin.* **8**, 129–146. <https://doi.org/10.1016/j.cpet.2013.02.001> (2013).
- Chaumeil, M. M., Lupo, J. M. & Ronen, S. M. Magnetic resonance (MR) metabolic imaging in glioma. *Brain Pathol.* **25**, 769–780. <https://doi.org/10.1111/bpa.12310> (2015).
- Rothman, D. L. *et al.* In vivo (^{13}C) and (^1H) - (^{13}C) MRS studies of neuroenergetics and neurotransmitter cycling, applications to neurological and psychiatric disease and brain cancer. *NMR Biomed.* **32**, e4172. <https://doi.org/10.1002/nbm.4172> (2019).
- Nelson, S. J. *et al.* Serial analysis of 3D H-1 MRSI for patients with newly diagnosed GBM treated with combination therapy that includes bevacizumab. *J. Neurooncol.* **130**, 171–179. <https://doi.org/10.1007/s11060-016-2229-3> (2016).
- Verma, G. *et al.* Three-dimensional echo planar spectroscopic imaging for differentiation of true progression from pseudoprogression in patients with glioblastoma. *NMR Biomed.* **32**, e4042. <https://doi.org/10.1002/nbm.4042> (2019).
- Ardenkjaer-Larsen, J. H. *et al.* Increase in signal-to-noise ratio of $> 10,000$ times in liquid-state NMR. *Proc. Natl. Acad. Sci. U.S.A.* **100**, 10158–10163 (2003).
- Comment, A. & Merritt, M. E. Hyperpolarized magnetic resonance as a sensitive detector of metabolic function. *Biochemistry* **53**, 7333–7357 (2014).
- Venkatesh, H. S. *et al.* Reduced phosphocholine and hyperpolarized lactate provide magnetic resonance biomarkers of PI3K/Akt/mTOR inhibition in glioblastoma. *Neuro Oncol.* **14**, 315–325. <https://doi.org/10.1093/neuonc/nor209> (2012).
- Chaumeil, M. M. *et al.* Hyperpolarized ^{13}C MR spectroscopic imaging can be used to monitor Everolimus treatment in vivo in an orthotopic rodent model of glioblastoma. *Neuroimage* **59**, 193–201. <https://doi.org/10.1016/j.neuroimage.2011.07.034> (2012).
- Chaumeil, M. M. *et al.* Hyperpolarized (^{13}C) MR imaging detects no lactate production in mutant IDH1 gliomas: Implications for diagnosis and response monitoring. *NeuroImage Clin.* **12**, 180–189. <https://doi.org/10.1016/j.nicl.2016.06.018> (2016).
- Capozzi, A. *et al.* Gadolinium effect at high-magnetic-field DNP: 70% (^{13}C) polarization of $[\text{U}-(^{13}\text{C})]$ glucose using trityl. *J. Phys. Chem. Lett.* **10**, 3420–3425. <https://doi.org/10.1021/acs.jpcclett.9b01306> (2019).
- Kurhanewicz, J. *et al.* Hyperpolarized (^{13}C) MRI: Path to clinical translation in oncology. *Neoplasia* **21**, 1–16. <https://doi.org/10.1016/j.neo.2018.09.006> (2019).
- Nelson, S. J. *et al.* Metabolic imaging of patients with prostate cancer using hyperpolarized $[\text{1-}(^{13}\text{C})\text{pyruvate}]$. *Sci. Transl. Med.* **5**, 198ra108. <https://doi.org/10.1126/scitranslmed.3006070> (2013).
- Gordon, J. W. *et al.* Translation of Carbon-13 EPI for hyperpolarized MR molecular imaging of prostate and brain cancer patients. *Magn. Reson. Med.* <https://doi.org/10.1002/mrm.27549> (2018).
- Miloushev, V. Z. *et al.* Metabolic imaging of the human brain with hyperpolarized (^{13}C) pyruvate demonstrates (^{13}C) lactate production in brain tumor patients. *Cancer Res.* **78**, 3755–3760. <https://doi.org/10.1158/0008-5472.CAN-18-0221> (2018).
- Mammoli, D. *et al.* Kinetic modeling of hyperpolarized carbon-13 pyruvate metabolism in the human brain. *IEEE Trans. Med. Imaging* <https://doi.org/10.1109/TMI.2019.2926437> (2019).
- Kennedy, B. W., Kettunen, M. I., Hu, D. E. & Brindle, K. M. Probing lactate dehydrogenase activity in tumors by measuring hydrogen/deuterium exchange in hyperpolarized $[\text{1-}(^{13}\text{C})\text{U-}(^2\text{H})\text{lactate}]$. *J. Am. Chem. Soc.* **134**, 4969–4977. <https://doi.org/10.1021/ja300222e> (2012).

28. Lai, M. *et al.* In vivo characterization of brain metabolism by (1) H MRS, (13) C MRS and (18) FDG PET reveals significant glucose oxidation of invasively growing glioma cells. *Int. J. Cancer* **143**, 127–138. <https://doi.org/10.1002/ijc.31299> (2018).
29. Rodrigues, T. B. *et al.* Magnetic resonance imaging of tumor glycolysis using hyperpolarized ¹³C-labeled glucose. *Nat. Med.* **20**, 93–97. <https://doi.org/10.1038/nm.3416> (2014).
30. Mishkovsky, M. *et al.* Measuring glucose cerebral metabolism in the healthy mouse using hyperpolarized (13)C magnetic resonance. *Sci. Rep.* **7**, 11719. <https://doi.org/10.1038/s41598-017-12086-z> (2017).
31. Cheng, T. *et al.* Automated transfer and injection of hyperpolarized molecules with polarization measurement prior to in vivo NMR. *NMR Biomed.* **26**, 1582–1588. <https://doi.org/10.1002/nbm.2993> (2013).
32. Hyacinthe, J. N. *et al.* Evaluating the potential of hyperpolarised [1-(13)C] L-lactate as a neuroprotectant metabolic biosensor for stroke. *Sci. Rep.* **10**, 5507. <https://doi.org/10.1038/s41598-020-62319-x> (2020).
33. Maher, E. A. *et al.* Metabolism of [U-13 C]glucose in human brain tumors in vivo. *NMR Biomed.* **25**, 1234–1244. <https://doi.org/10.1002/nbm.2794> (2012).
34. Linnik, I. V. *et al.* Noninvasive tumor hypoxia measurement using magnetic resonance imaging in murine U87 glioma xenografts and in patients with glioblastoma. *Magn. Reson. Med.* **71**, 1854–1862. <https://doi.org/10.1002/mrm.24826> (2014).
35. Denko, N. C. Hypoxia, HIF1 and glucose metabolism in the solid tumour. *Nat. Rev. Cancer* **8**, 705–713. <https://doi.org/10.1038/nrc2468> (2008).
36. Mathivet, T. *et al.* Dynamic stroma reorganization drives blood vessel dysmorphia during glioma growth. *EMBO Mol. Med.* **9**, 1629–1645. <https://doi.org/10.15252/emmm.201607445> (2017).
37. Hovhannisyian, N. *et al.* [(18)F]Fludarabine-PET as a promising tool for differentiating CNS lymphoma and glioblastoma: Comparative analysis with [(18)F]FDG in human xenograft models. *Theranostics* **8**, 4563–4573. <https://doi.org/10.7150/thno.26754> (2018).
38. Doblas, S. *et al.* In vivo characterization of several rodent glioma models by ¹H MRS. *NMR Biomed.* **25**, 685–694. <https://doi.org/10.1002/nbm.1785> (2012).
39. Najac, C. & Ronen, S. M. MR molecular imaging of brain cancer metabolism using hyperpolarized ¹³C magnetic resonance spectroscopy. *Top. Magn. Reson. Imaging* **25**, 187–196. <https://doi.org/10.1097/RMR.000000000000104> (2016).
40. Mair, R. *et al.* Metabolic imaging detects low levels of glycolytic activity that vary with levels of c-Myc expression in patient-derived xenograft models of glioblastoma. *Cancer Res.* **78**, 5408–5418. <https://doi.org/10.1158/0008-5472.CAN-18-0759> (2018).
41. Stine, Z. E., Walton, Z. E., Altman, B. J., Hsieh, A. L. & Dang, C. V. MYC, metabolism, and cancer. *Cancer Discov.* **5**, 1024–1039. <https://doi.org/10.1158/2159-8290.CD-15-0507> (2015).
42. Lu, M., Zhu, X. H., Zhang, Y., Mateescu, G. & Chen, W. Quantitative assessment of brain glucose metabolic rates using in vivo deuterium magnetic resonance spectroscopy. *J. Cereb. Blood Flow Metab.* **37**, 3518–3530. <https://doi.org/10.1177/0271678X17706444> (2017).
43. De Feyter, H. M. *et al.* Deuterium metabolic imaging (DMI) for MRI-based 3D mapping of metabolism in vivo. *Sci. Adv.* **4**, eaat7314. <https://doi.org/10.1126/sciadv.aat7314> (2018).
44. Granlund, K. L. *et al.* Hyperpolarized MRI of human prostate cancer reveals increased lactate with tumor grade driven by monocarboxylate transporter 1. *Cell Metab.* **31**, 105–114 e103. <https://doi.org/10.1016/j.cmet.2019.08.024> (2020).
45. Gallagher, F. A. *et al.* Imaging breast cancer using hyperpolarized carbon-13 MRI. *Proc. Natl. Acad. Sci. U.S.A.* **117**, 2092–2098. <https://doi.org/10.1073/pnas.1913841117> (2020).
46. Rao, Y. *et al.* Hyperpolarized [1-(13)C]pyruvate-to-[1-(13)C]lactate conversion is rate-limited by monocarboxylate transporter-1 in the plasma membrane. *Proc. Natl. Acad. Sci. U.S.A.* **117**, 22378–22389. <https://doi.org/10.1073/pnas.2003537117> (2020).
47. Eichhorn, T. R. *et al.* Hyperpolarization without persistent radicals for in vivo real-time metabolic imaging. *Proc. Natl. Acad. Sci. U.S.A.* **110**, 18064–18069. <https://doi.org/10.1073/pnas.1314928110> (2013).
48. Capozzi, A., Cheng, T., Boero, G., Roussel, C. & Comment, A. Thermal annihilation of photo-induced radicals following dynamic nuclear polarization to produce transportable frozen hyperpolarized (13)C-substrates. *Nat. Commun.* **8**, 15757. <https://doi.org/10.1038/ncomms15757> (2017).
49. Capozzi, A. *et al.* Efficient hyperpolarization of U-(13) C-glucose using narrow-line UV-generated labile free radicals. *Angew. Chem.* **58**, 1334–1339. <https://doi.org/10.1002/anie.201810522> (2019).
50. Sciuscio, D. *et al.* Extent and patterns of MGMT promoter methylation in glioblastoma- and respective glioblastoma-derived spheres. *Clin. Cancer Res.* **17**, 255–266. <https://doi.org/10.1158/1078-0432.CCR-10-1931> (2011).
51. Bady, P. *et al.* DNA fingerprinting of glioma cell lines and considerations on similarity measurements. *Neuro Oncol.* **14**, 701–711. <https://doi.org/10.1093/neuonc/nos072> (2012).
52. Vassallo, I. *et al.* WIF1 re-expression in glioblastoma inhibits migration through attenuation of non-canonical WNT signaling by downregulating the lncRNA MALAT1. *Oncogene* **35**, 12–21. <https://doi.org/10.1038/onc.2015.61> (2016).
53. Cheng, T., Capozzi, A., Takado, Y., Balzan, R. & Comment, A. Over 35% liquid-state ¹³C polarization obtained via dissolution dynamic nuclear polarization at 7 T and 1 K using ubiquitous nitroxyl radicals. *Phys. Chem. Chem. Phys.* **15**, 20819–20822. <https://doi.org/10.1039/c3cp53022a> (2013).
54. Comment, A. *et al.* Design and performance of a DNP prepolarizer coupled to a rodent MRI scanner. *Concept Magn. Reson. B* **31B**, 255–269. <https://doi.org/10.1002/cmrb.20099> (2007).
55. Gruetter, R. & Tkac, I. Field mapping without reference scan using asymmetric echo-planar techniques. *Magn. Reson. Med.* **43**, 319–323. [https://doi.org/10.1002/\(SICI\)1522-2594\(200002\)43:2%3c319::AID-MRM22%3e3.0.CO;2-1\[pil\]](https://doi.org/10.1002/(SICI)1522-2594(200002)43:2%3c319::AID-MRM22%3e3.0.CO;2-1[pil]) (2000).
56. Mlynarik, V., Gambarota, G., Frenkel, H. & Gruetter, R. Localized short-echo-time proton MR spectroscopy with full signal-intensity acquisition. *Magn. Reson. Med.* **56**, 965–970. <https://doi.org/10.1002/mrm.21043> (2006).
57. Provencher, S. W. Estimation of metabolite concentrations from localized in vivo proton NMR spectra. *Magn. Reson. Med.* **30**, 672–679 (1993).
58. Porcari, P. *et al.* Early detection of human glioma sphere xenografts in mouse brain using diffusion MRI at 14.1 T. *NMR Biomed.* **29**, 1577–1589. <https://doi.org/10.1002/nbm.3610> (2016).

Acknowledgements

We thank Drs. Magnus Karlsson and Mathilde H Lerche for assistance with the DNP sample formulation. This work was supported by the Swiss National Science Foundation (Grant PP00P2_133562 to A.C.; 31003A_163297 and 31003A_138116 to M.E.H.). We thank the Centre d’Imagerie BioMédicale (CIBM) of the UNIL, UNIGE, HUG, CHUV, EPFL, and the Leenards and Jeantet Foundations.

Author contributions

M.M., O.G., and M.E.H. designed and supervised the project. O.G., I.V., and M.F.H. prepared the animals, JB provided fresh human tumor samples. M.M. and A.C. designed the HP MRS experiments. M.M. and C.C. designed the proton MRS measurements. M.M. acquired the MR data. M.M., O.G., B.L., R.G., and M.E.H.

interpreted and/or reviewed the data. M.M., O.G., B.L., M.E.H. wrote the manuscript. All authors approved the content of this paper.

Competing interests

Dr. Arnaud Comment was employed by General Electric Medical Systems Inc. at the time of manuscript preparation and submission. All other authors declare no competing interest.

Additional information

Supplementary Information The online version contains supplementary material available at <https://doi.org/10.1038/s41598-021-85339-7>.

Correspondence and requests for materials should be addressed to M.M. or M.E.H.

Reprints and permissions information is available at www.nature.com/reprints.

Publisher's note Springer Nature remains neutral with regard to jurisdictional claims in published maps and institutional affiliations.



Open Access This article is licensed under a Creative Commons Attribution 4.0 International License, which permits use, sharing, adaptation, distribution and reproduction in any medium or format, as long as you give appropriate credit to the original author(s) and the source, provide a link to the Creative Commons licence, and indicate if changes were made. The images or other third party material in this article are included in the article's Creative Commons licence, unless indicated otherwise in a credit line to the material. If material is not included in the article's Creative Commons licence and your intended use is not permitted by statutory regulation or exceeds the permitted use, you will need to obtain permission directly from the copyright holder. To view a copy of this licence, visit <http://creativecommons.org/licenses/by/4.0/>.

© The Author(s) 2021